Mass diffusion and Soret coefficient measurements of triethylene glycol/water binary mixtures by dynamic shadowgraphy

A T Ndjaka, L. García-Fernández, Dan-Esli Bouyou Bouyou, A. Lassin, M. Azaroual, F. Croccolo, H. Bataller

Eur. Phys. J. E _####################_
https://doi.org/10.1140/epje/s10189-022-00171-9

THE EUROPEAN PHYSICAL JOURNAL E

Regular Article - Flowing Matter

Mass diffusion and Soret coefficient measurements of triethylene glycol/water binary mixtures by dynamic shadowgraphy

A. T. Ndjaka[1,2], L. García-Fernández[3], D. E. Bouyou Bouyou[1], A. Lassin[2], M. Azaroual[2,4], F. Croccolo[1], and H. Bataller[1,a]

[1] E2S UPPA, CNRS, TotalEnergies, LFCR, Universite de Pau et des Pays de l'Adour, UMR5150, Anglet, France
[2] BRGM, F-45060 Orléans, France
[3] Department of Structure of Matter, Thermal Physics and Electronics, Faculty of Physics, University Complutense of Madrid, Avda. Complutense s/n,, 28040 Madrid, Spain
[4] CNRS, BRGM, ISTO, Univ. Orléans, UMR 7327, F-45071 Orléans, France

Received 23 November 2021 / Accepted 8 February 2022

Abstract The investigation of the transport properties of binary fluid mixtures remains a topic of interest in relation to the more challenging studies of ternary mixtures. In fact, the study of the phase boundary limits of the Gibbs composition triangle can be the initial step for a more complete analysis of ternary mixtures. In this paper, we apply the dynamic shadowgraphy optical technique to study non-equilibrium fluctuations induced by the presence of a gradient of temperature and/or of concentration in the triethylene glycol (TEG)/water system. These thermodiffusion and free-diffusion experiments aim at measuring the transport properties of samples of the studied system at different experimental conditions. We scan both the average temperature and the TEG concentration, which allows us investigating both positive and negative thermodiffusive behaviours. The obtained values of mass diffusion coefficient are consistent with data available in the literature in the range of temperature investigated in this study. The mass diffusion coefficient of the sample prepared at 0.7 w/w TEG concentration are characterised by shadowgraphy following the two proposed methods, exhibiting consistent results. An increase of the mass diffusion coefficient as a function of the average temperature is highlighted. On the other hand, the thermodiffusion coefficient appears to be independent of the average temperature of the sample at 0.3 w/w TEG concentration.

1 Introduction

The transport properties of complex fluids under non-equilibrium conditions are of interest from both scientific and technological points of view. Transport phenomena occurs in almost any multicomponent mixture present in nature and in industry and its comprehension is of great interest for many applications, such as the exploitation of crude oil wells and the storage of CO_2 in deep brine aquifers. [1,2]. A suitable characterization of transport processes in complex mixtures requires a thorough understanding of simpler fluids. So far, binary mixtures have been extensively characterized [3,4]. The extension of theories and experiments from binary to ternary mixtures requires further development due to the intrinsic and significant increase of difficulty with the number of components of the mixture and their mutual interactions. Currently, a great effort is devoted to investigate the transport phenomena in ternary mixtures. Thermodiffusion experiments in ternary mixtures are performed on ground, by using different optical techniques [3,5–7], or in microgravity conditions in order to avoid both convection and sedimentation. The thermodynamic characterization of ternary mixtures is one of the objectives of different ESA projects, like: Diffusion Coefficient Measurements in ternary mIXtures (DCMIX) [7–11], Soret Coefficients in Crude Oil (SCCO) [12–15] and Giant Fluctuations [16,17]. The knowledge of the behavior of the binaries associated to the ternaries remains an important step because they correspond to the binary phase boundary limits in the ternary Gibbs composition triangle, and interpolated values of the Soret coefficient can be obtained in some conditions [18].

Complex fluids subjected to non-equilibrium conditions exhibit non-equilibrium fluctuations (NEFs) of the thermodynamic variables [19–23]. These conditions

T.I. : Thermal non-equilibrium phenomena in fluid mixtures. Guest editors: Fernando Bresme, Bjørn Hafskjold, Werner Köhler, Francois Montel

[a] e-mail: henri.bataller@univ-pau.fr (corresponding author)

can be induced, for example, by applying a temperature gradient to a multicomponent fluid mixture, thus inducing a temperature gradient within the fluid as well as a composition gradient by means of thermodiffusion, also called the Soret effect [3,24]. Superimposing two layers at different concentrations of a solution generates an initial gradient of concentration which evolves towards an equilibrium state by mass diffusion, in the absence of convective motions [25]. Both free-diffusion and thermodiffusion transport processes can be investigated by optical techniques and particularly by light scattering thanks to its ability to visualize NEFs without altering the intrinsic properties of the fluid. The transport properties of the fluid can be determined both at atmospheric [26,27] and at high pressure [28]. In this work, dynamic shadowgraphy has been adopted [25,29,30] to study the refractive index fluctuations as generated by the NEFs of the temperature and concentration in the case of thermodiffusion experiments, and of the concentration in the case of free-diffusion experiments. It is important to highlight the novelty of using this methodology to determine the transport properties of fluid mixtures in free-diffusion experiments. By shadowgraphy, a large range of fluctuation sizes λ or, conversely, of wave numbers $q = 2\pi/\lambda$, can be investigated at the same time, providing simultaneous reliable measurements of different transport properties, like mass diffusion coefficient or thermal diffusivity as well as Soret coefficient [5,26,31].

The aim of the present work is to investigate the diffusion and the thermodiffusion coefficients of the binary mixture of triethylene glycol (TEG) and water (H_2O), as one of the binary limits of the DCMIX3 ternary system, made of H_2O, ethanol and TEG [11]. These molecules are highly polar, and the prevailing hydrogen bonding leads to much more complex interactions than the dominating dispersion interactions in alkane mixtures for example, leading to negative values of the Soret coefficient and to convective instabilities under terrestrial gravity conditions. In this study, it is worth noting the possibility of characterising mixtures with negative Soret coefficients through the analysis of NEFs by using shadowgraph technique in both thermodiffusion and free-diffusion experiments.

The remainder of this paper is organized as follows: in Sect. 2, the experimental procedure is described. In Sect. 3, the theory of non-equilibrium fluctuations is summarized to provide the relevant working equations. The obtained results are presented in Sect. 4, finally, conclusions are provided in Sect. 5.

2 Experimental procedure

2.1 Solutions preparation and characterisation

Triethylene glycol (Sigma-Aldrich, T59455-1L, ReagentPlus®, purity 99%), used without further purification, and degassed de-ionized water (resistivity 18.5 MΩcm), retrieved from a Millipore Milli-Q filtration station, were used to prepare the studied samples at the required mixture compositions using an analytical balance (Sartorius TE313S, resolution 10^{-2} g/200 g). The thermophysical properties of the mixture, such as density, viscosity and both thermal and mass expansion coefficients are measured as follows.

The kinematic viscosity ν is measured at 20, 25 and 30 °C by capillary viscometer (Ubbelohde SCHOTT). The thermal and solutal expansion coefficients α and β, respectively, are defined as follows:

$$\alpha = -\frac{1}{\rho}\left(\frac{\partial \rho}{\partial T}\right)_{C,p} \quad (1)$$

$$\beta = \frac{1}{\rho}\left(\frac{\partial \rho}{\partial C}\right)_{T,p} \quad (2)$$

where ρ is the mixture density, T is the temperature and C is the TEG concentration in mass fraction.

The coefficients α and β are indirectly determined from measurements of the mixture density performed at different conditions through a Density Meter (ANTON PAAR, DMA 5000). First, in order to determine the thermal expansion coefficient, the density is measured at different temperatures (starting from 2 °C below the nominal temperature up to 2 °C above), while keeping the concentration constant. A linear relationship between the density and the temperature is observed in all cases. The parameter α is determined through Eq. (1), i.e. dividing the slope of the density vs. temperature by the density of the sample at the nominal temperature. Second, the mass expansion coefficient is obtained after measuring the density at different concentrations (starting from 2% w/w below the nominal concentration up to 2% w/w above), while keeping the temperature constant. A linear relationship between the density and the concentration is observed in all cases. The parameter β is determined through Eq. (2), i.e. dividing the slope of the density vs. concentration by the density of the sample at the nominal concentration. Measured values of ν, α and β are summarized in Table 1.

The measurements of viscosity and density are repeated at least three times for each sample. The viscosities reported in Table 1 are calculated as the average of the three measurements and the corresponding uncertainties are the standard deviations. Considering the density uncertainties and the sensitivity of the method of least-square adjustment, the uncertainties on α and β are calculated by error propagation.

2.2 Free-diffusion and thermodiffusion cells

For the free-diffusion experiments, we used a diffusion cell specifically designed to put into contact two layers of two different liquid mixtures or two solutions of the same components at different concentrations, thus creating an initial step concentration gradient at uniform temperature while providing vertical optical access to a central area of the cell, similar to the flowing-junction cell already reported in the literature [32]. The diffusion

Table 1 Kinematic viscosity ν,thermal expansion coefficient $\alpha$and solutal expansion coefficient β at different both mass fraction concentrations C of TEG and temperatures T

$T(^\circ$ C)	ν (mm^2/s)	α ($\times$ 10^{-4} K^{-1})	β ($\times$ 10^{-1})
$C = 0.3$ w/w			
20	2.72 ± 0.03	4.22 ± 0.02	1.59 ± 0.08
25	2.32 ± 0.02	4.49 ± 0.02	1.55 ± 0.07
30	2.01 ± 0.02	4.77 ± 0.02	1.51 ± 0.07
$C = 0.5$ w/w			
20	6.25 ± 0.06	5.77 ± 0.01	0.145 ± 0.009
25	5.20 ± 0.05	5.87 ± 0.01	0.138 ± 0.005
30	4.34 ± 0.04	6.02 ± 0.01	0.134 ± 0.003
$C = 0.7$ w/w			
20	14.8 ± 0.1	6.633 ± 0.007	0.96 ± 0.02
25	11.9 ± 0.1	6.712 ± 0.004	0.949 ± 0.006
30	9.7 ± 0.1	6.799 ± 0.005	0.938 ± 0.008

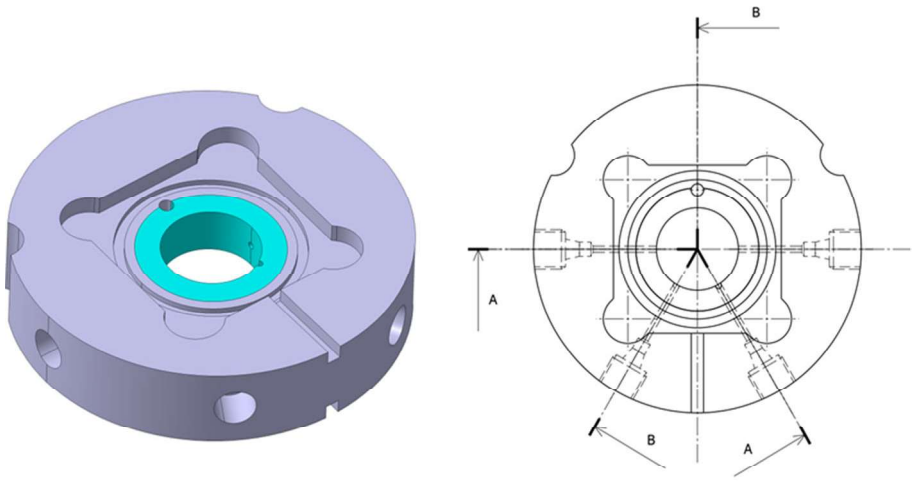

Fig. 1 **a** 3D-drawing of the stainless steel annulus with the Teflon ring in the inner part. **b** 2D-drawing of the same, as observed from the top

cell consists of a stainless steel annulus (see Fig. 1) with internal and external diameters of 30 mm and 80 mm, respectively, and a vertical thickness of $h = 10$ mm. The metallic annulus hosts four holes: two for fluids outlets at 180° in the horizontal plane and at mid-height of the cell in the vertical direction, and two for fluid inlet at 50°in the horizontal plane and at the same height in the vertical direction. In order to avoid the thermal contact between the liquid sample and the interior of the conductive metallic annulus, a polytetrafluoroethylene (Teflon®) ring with an internal and external diameter of 20 mm and 30 mm, respectively, is placed inside the stainless steel annulus (see Fig. 1a) . This ring has also four thin holes in correspondence to those present in the metallic annulus to allow the circulation of the fluids. Moreover, the two holes for the fluid inlets are inclined in the vertical direction so that one incoming fluid is steered to the top of the cell, while the other one is steered to the bottom of the cell.

The stainless steel annulus is designed to accommodate two square sapphire windows ($8\times40\times40$ mm^3), one on each vertical side with a groove for a Viton®O-ring for sealing. The two internal faces of the two sapphire windows are then separated by the metal annulus and kept apart by $h = 10$ mm, thus defining the vertical thickness of the fluid sample. The external surfaces of the two sapphire windows are in contact with two square aluminium plates with a central circular aperture with a diameter $d = 13$ mm. These plates are meant for hosting two temperature sensors so to measure the temperature as close as possible to the sapphires. The aluminium plates are also in contact with two square Peltier elements (Kryotherm, TB-109-1.4-1.5 CH) which can transport heat by means of a current flow and have the same central circular aperture. The Peltier elements provide/remove the heat necessary to maintain the set-point temperature as driven by two temperature controllers (Wavelength Electronics, LFI-3751) which use a proportional-integrating-derivative feedback system and maintain the temperature of the internal side of each Peltier device constant, with stability better than 1 mK RMS over 1 day. As shown in Fig. 2, all these elements are clamped by means of two aluminium blocks (with the same central circular aperture) in which water coming from a thermostatic controlled bath (Huber, ministat 125), circulates in order to remove the Peltier elements excess heat.

Journal: **10189** MS: **0171** ☐ TYPESET ☐ DISK ☐ LE ☐ CP Disp.:**2022/2/24** Pages: **15** Layout: **EPJE**

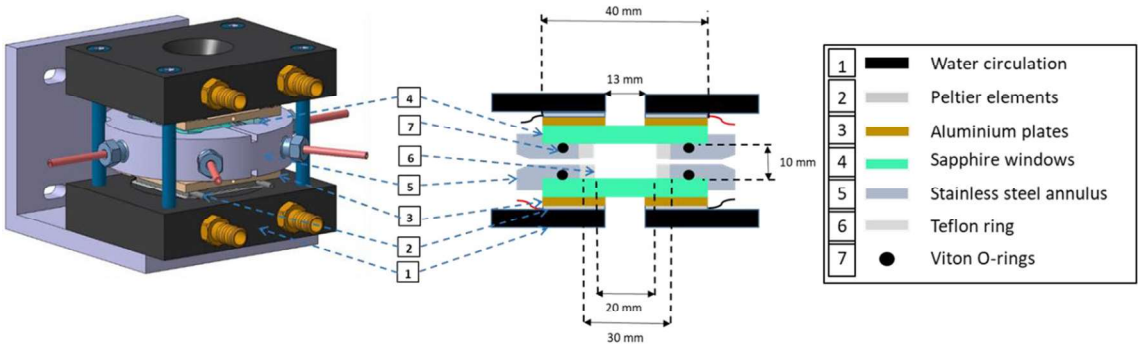

Fig. 2 3D drawing of the free-diffusion cell

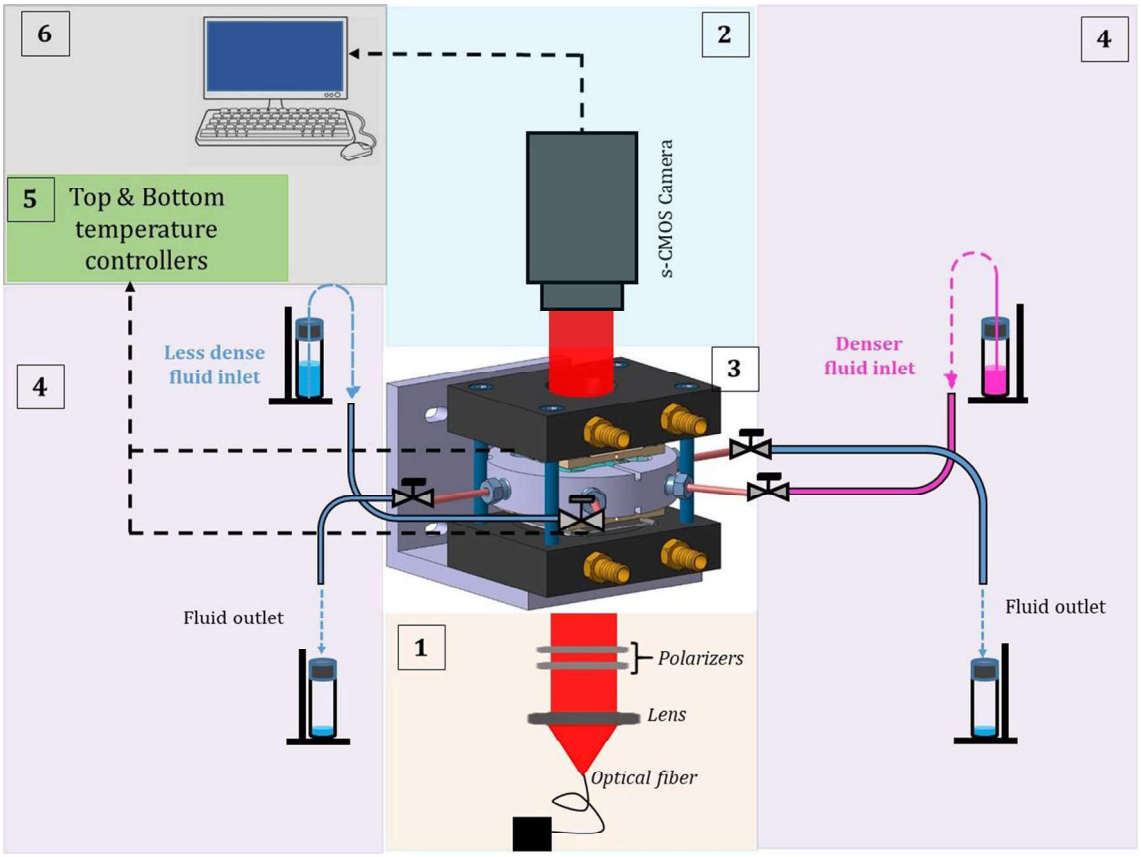

Fig. 3 Shadowgraph optical set up summarized in six distinct blocks: **1** optical components; **2** s-CMOS Camera; **3** free-diffusion/thermodiffusion cell; **4** specific filling procedure; **5** temperature controllers; **6** computer equipment

External to the stainless steel ring, metallic capillary tubes with external diameter of 1/8 inch and about 50 mm of length (the red stems visible in Fig. 2) are connected to each inlet/outlet. These capillary tubes end with a manual valve each (Swagelok, SS-41GS2), as shown in Fig. 3. The sample reservoirs are connected to the valves via flexible capillary tube (same external diameter as the metallic capillary tubes).

The cell filling is performed in two main steps. In the first step, the diffusion cell is completely filled with the less dense fluid. In order to do that, the fluid is slowly injected by gravity through the lower part, while air is let out of the outlet pointing to the top. By slightly tilting the cell, the residual air can be completely removed. Attention is paid to avoid any further air inlet while filling the other three capillary tubes. The second step consists of filling the bottom half of the cell with the denser fluid and create a sharp interface between the two fluids. This is achieved by filling the cell simultaneously with the two fluids from the bottom and the top inlets, while the remixed fluid is let out through the two outlets. Once half of the cell is filled with the denser fluid (the volume of fluid to be injected into the cell to fill it by half, taking into account the length and the internal diameter of capillary tubes and the dead volumes is calculated beforehand), a relatively flat horizontal interface between the two fluids is formed. The four

valves are simultaneously closed and the free-diffusion process starts.

For the thermodiffusion experiments the stainless steel annulus is replaced by a Viton O-ring with an internal diameter of $d = 25$ mm and thickness of $e = 3$ mm, the other components remain unchanged and capillaries are not necessary. The two sapphire windows are kept apart by four plastic spacers of $h = 2.00 \pm 0.01$ mm, thus defining the liquid layer thickness. The cell is filled by means of two syringe needles punctured through the Viton O-ring. During the filling procedure, the cell is inclined and the fluid is pushed through the bottom syringe while air is removed through the top one. After filling, the two needles are carefully removed and the holes in the O-ring close due to the pressure exercised on it by the sapphire windows. The cell is inserted into the shadowgraph setup once the filling is finished. For any given mean temperature, a temperature difference between the top and the bottom is applied by setting the corresponding temperatures to the Peltier elements. Once the stationary state is reached, i.e. after one diffusive time for the cell, the image recording is started.

2.3 Shadowgraph setup

The shadowgraph optical setup (Fig. 3) involves a super luminescent diode (Super Lumen, SLD MS-261-MP2-SM, $\lambda = 675 \pm 13$ nm), connected to a single-mode optical fiber. The divergent beam at the output of the fiber is collimated by an achromatic doublet lens (focal length $f = 150$ mm, and diameter $\phi = 50.8$ mm). The collimated beam passes through the free-diffusion cell, or the thermodiffusion cell, via two linear polarizers that allow adjusting the average transmitted light intensity, and is supposed to be perpendicular to the interface between the two solutions, in the case of free diffusion experiments, or parallel to the temperature gradient in the case of thermodiffusion experiments. A camera, whose detection plane is positioned at a distance of $z = (12.0 \pm 0.5)$ cm from the sample central plane, collects the sum of the light scattered by the NEFs plus the transmitted one. As a camera sensor, we use a scientific-CMOS camera (Hamamatsu Digital Camera C13440, ORCA - Flash 4.0 V3) whose detector size is $s = 13.3$ mm. This camera sensor allows a fast image acquisition frequency, up to 100 Hz at full frame resolution of 2048×2048 square pixels with a pixel side of $l_{pix} = 6.5$ µm. Images are acquired in real time by the HCImageLive (x64) software program installed in a dedicated PC. In order to have both a good stability of acquisition frequency and a quick backup of the images, we use 4 Solid-State Drive (SSD) hard disks in RAID0 configuration.

2.4 Dynamic near field imaging

The images acquired in the near field consist of an intensity map $I(\vec{x}t)$, generated by the interference on the s-CMOS plane between the portion of the incident beam that has passed undisturbed through the sample and the beams scattered by the refractive index fluctuations occurring within the sample. Here, $\vec{x}$ and t stand for the position in the image plane and the time lapsed during the acquisition, respectively. Thanks to the interference of different beams, the fluctuations in the fluid density, that are proportional to the fluctuations of the fluid refractive index, are transformed into fluctuations of the light intensity at the detector plane. Therefore, in order to study the dynamics of the density fluctuations in our samples, we calculate the Structure Function (SF) of the light intensity, i.e. of the acquired images, by means of an already proven Differential Dynamic Algorithm (DDA) [33]. The DDA algorithm consists of the following main steps: first, each recorded image $I(\vec{x}t)$ is Fourier transformed in the 2D spatial space of the detector plane to obtain $I(\vec{q},t) = \mathcal{F}(I(\vec{x},t))$, then the Fourier transform (FT) is normalised by dividing it by the zero spatial frequency $\mathrm{i}(\vec{q},t) = I(\vec{q},t)/I\left(\vec{0},t\right)$ in order to remove the source intensity fluctuations. Then, the differences between normalized FTs at a given time difference Δt (called correlation time) $\Delta i(\vec{q},t,\Delta t) = i(\vec{q},t) - i(\vec{q},t+\Delta t)$ are calculated. These $\Delta t's$ are, of course, multiples of the time delay $\mathrm{d}t_{min}$ of the recording process, and cannot be larger than the acquisition duration. Finally, the 2D correlation functions are calculated by determining the - square moduli $|\Delta i(\vec{q},t,\Delta t)|^2$ of the FT differences, and the individual spatial Fourier transforms of the image differences are averaged, first over all times $t$and second over the modulus of the wave number $\vec{q}$ over the azimuthal angle. The result $\langle|\Delta i(q,\Delta t)|^2\rangle_{q,t}$ is the SF of the recorded intensity fluctuations. In order to reduce the computational time to calculate the structure function out of the image series, we make use of a graphic card with the advantage of the massive parallelization on the Graphic Processing Unit (GPU) and an in-house developed software [33,34]. This experimental quantity requires a physical model for its interpretation. The details of the theoretical model can be found elsewhere [19,20]. In the present paper, we just recall the essential equations used to fit the SF.

2.5 Structure function analysis

The SF can be related to the power spectrum density fluctuation and the characteristics of the optical system as follows:

$$\langle|\Delta i(q,\Delta t)|^2\rangle = 2\{T(q)S(q)[1 - ISF(q,\Delta t)] + B(q,\Delta t)\} \quad (3)$$

where $T(q)$ is the optical transfer function of the shadowgraph, $S(q)$ the static power spectrum of the fluctuations, the product $A(q) = T(q)S(q)$ is called the static structure factor (independent of the correlation time) and $B(q,\Delta t)$ is the signal background. It includes different contributions like electronic noise due to the camera and all the acquisition chain and can be modelled by

$B(q,\Delta t) = C(q) + E(q)\cdot\Delta t + F(q)\cdot\Delta t^2$ The parabolic term $F(q)\cdot\Delta t^2$ becomes particularly important for the experiments performed in the free-diffusion configuration, where the system is never at the steady state, so that the background noise becomes time-dependent. The Intermediate Scattering Function $ISF(q,\Delta t)$ corresponds to the dynamic part of the SF, that can be described in many cases as the sum of exponential decays [35–37]: $ISF(q,\Delta t) = \sum_i a_i exp\left(-\Delta t/\tau_i(q)\right)$, where a_i are the amplitudes of the different modes with $\sum_i a_i = 1$ and $\tau_i(q)$ the wave-number-dependent relaxation times.

During a free-diffusion experiment, the density fluctuations recorded through the shadowgraph are mostly due to concentration-NEFs (c-NEFs) that are much more intense (orders of magnitude) than equilibrium temperature and/or concentration fluctuations present at the same time for the wave number range of our interest. Thus, the *ISF* is expected to be well described by a single exponential decay for all wave numbers. Thus, the SF is supposed to take the following form:

$$\langle|\Delta i(q,\Delta t)|^2\rangle = 2\Bigg\{A(q)\left[1-\exp\left(-\frac{\Delta t}{\tau_c(q)}\right)\right] + C(q) + E(q)\cdot\Delta t + F(q)\cdot\Delta t^2\Bigg\} \quad (4)$$

where $\tau_c(q)$ is the decay time of the c-NEFs at wave number q.

When a stable temperature gradient parallel to the gravity field is applied to a homogenous binary fluid mixture, a concentration gradient is formed due to the Soret effect [3]. Hence, at the steady state of a thermodiffusion experiment a suitable expression for the *ISF* can be provided by the sum of two exponential decays given by the fluctuations of the concentration plus the fluctuations of the temperature (t-NEFs). The SF is supposed to take the following form:

$$\langle|\Delta i(q,\Delta t)|^2\rangle = 2\Bigg\{A(q)\left[1-\left\{a\times\exp\left(-\frac{\Delta t}{\tau_T(q)}\right) + (1-a)\times\exp\left(-\frac{\Delta t}{\tau_c(q)}\right)\right\}\right] + C(q) + E(q)\cdot\Delta t + F(q)\cdot\Delta t^2\Bigg\} \quad (5)$$

where $\tau_T(q)$ is the decay time of the t-NEFs at wave number q.

$A(q), \tau_i(q), C(q), E(q)$ and $F(q)$ are the fitting parameters at each wave number. In the case of a thermodiffusion experiment, if the steady state is fully reached, the term $F(q)$ is supposed to be negligible. However, we keep it in the fit in order to check the validity of our hypothesis and to be sure that the steady state has been reached. We use MATLAB and an implemented Levenberg-Marquad nonlinear least-square fitting routine [38]. At the end of the fitting, we proceed to the analysis of the statics of the fluctuations through the static structure factor $A(q)$, as well as to the analysis of the dynamics of the fluctuations through the decay times $\tau_i(q)$. In the present paper, we will focus on the dynamics of the fluctuations.

3 Dynamics of the non-equilibrium fluctuations

The details of the theoretical description of the hydrodynamic behaviour of density fluctuations out-of-equilibrium can be found elsewhere [19,20], so that here we just recall the main expressions useful for the experimental data analysis.

At intermediate and large wave numbers, in the absence of any convective movement, in the presence of the gravity force and in the bulk fluid, the decay time of the c-NEFs is given by:

$$\tau_c(q) = \frac{1}{Dq^2\left[1+\left(\frac{q_c}{q}\right)^4\right]} \quad (6)$$

where D is the mass diffusion coefficient and q_c the cut-off wave number which defines the length scale below which the dynamics of the c-NEFs are no longer dominated by diffusion, but rather by buoyancy. The curve of the decay times as a function of wave numbers looks like a bell-shape (in log-log scale) and mirrors the presence of two distinct regimes as already reported in a number of previous publications [25,26,39]. The asymptotic behaviour of Eq. 6 for wave numbers larger than q_c is $\tau_c(q) = 1/Dq^2$ so that the diffusion coefficient D can be obtained from the fitting of the experimental data points in this region. In the case of a thermodiffusion experiment, the cut-off wave number is given by the expression [26,28,31,40]:

$$q_c = \left(\frac{\beta g S_T C_0(1-C_0)\Delta T}{h\nu D}\right)^{1/4} \quad (7)$$

where β is the mass expansion coefficient of the binary mixture, g the gravitational acceleration, h is the vertical thickness of the sample, C_0 the equilibrium mass fraction of the denser component, S_T the Soret coefficient of the denser component, ΔT the difference of temperature between the top and the bottom of the thermodiffusion cell, and ν the kinematic viscosity of the binary mixture at the mean temperature of the experiment.

During a free-diffusion experiment, the concentration difference between the bottom and the top of the cell is assumed to remain constant until the diffusive process reaches the cell boundaries at the diffusive time $\tau_d =$

$(h/2)^2/\pi D$. For times smaller than τ_d the cut-off wave number is given by the expression [25,39,41]:

$$q_c = \left(\frac{\beta g\,(C_1 - C_2)}{\nu D\sqrt{4\pi D t}}\right)^{1/4} \tag{8}$$

where C_1 and C_2 are the concentrations of the denser component, TEG, at the bottom and top layers in the diffusion cell, respectively. Unlike the thermodiffusion experiment, the cut-off wave number is time-dependent, following a power law with a $(-1/8 = -0.125)$ exponent.

Again, here we recall only the essential equations that are used to model the t-NEFs in the case of thermodiffusion experiments.

At intermediate and large wave numbers, in the absence of convection, in the presence of the gravity force and in the bulk fluid, the decay time of the t-NEFs is given by:

$$\tau_T(q) = \frac{1}{a_T q^2\left[1 + \left(\frac{q_T}{q}\right)^4\right]} \tag{9}$$

where a_T is the thermal diffusivity and q_T the thermal cut-off wave number which defines the length scale below which the dynamics of the t-NEFs is no longer dominated by heat diffusion, but rather by buoyancy. The curve of the decay times as a function of wave numbers looks similar to the one described for c-NEFS, but, in general, decay times are shorter, due to the larger value of thermal diffusivity with respect to mass diffusion coefficient. The asymptotic behaviour of Eq. 9 for wave numbers larger than q_T is $\tau_T(q) = 1/(a_T q^2)$ so that the thermal diffusivity a_T can be obtained from the fitting of the experimental data points in this region.

4 Results and discussion

Mass diffusion and Soret coefficients for the mixture TEG/water at different concentrations are already known in the literature [42]. The present paper is intended to bring new measurements of the fluid transport properties at different temperatures. Some of the values reported here are anticipated in a joint paper about the system TEG/water/ethanol and the associated binary mixtures characterised by different measurement techniques [18]. Here we provide a full detailed description of the experiments performed in our laboratory by means of dynamic shadowgraphy and the analysis of NEFs.

4.1 Thermodiffusion experiments

One remarkable property of the TEG/water mixture is that the sign of the Soret coefficient changes with respect to concentration. This implies that under thermal stress the denser component (TEG) migrates towards either the hot plate or the cold one. For $C = 0.3$ w/w, the Soret coefficient is positive, so that the TEG migrates towards the cold plate, while for concentrations higher than $C = 0.5$ w/w the Soret coefficient is negative in the temperature range between 15 °C and 40 °C, so that the TEG accumulates at the hot plate. The presence of a negative Soret coefficient makes it difficult to perform thermodiffusion experiments in the presence of the gravitational field because, while heating the mixture from above, the density gradient generated by the concentration one (at the steady state of Soret separation) is unstable and can induce convection transport process in the system.

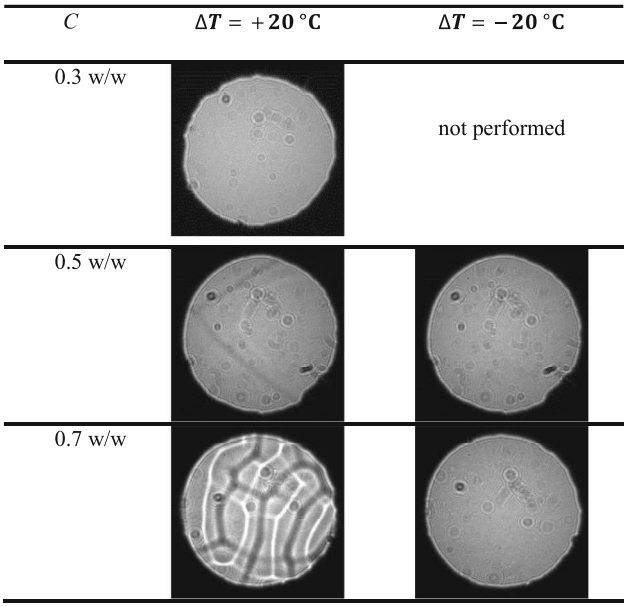

Fig. 4 Shadowgraph patterns obtained at a mean temperature of 25 °C after applying different temperature gradients to samples of TEG concentration C (from top to bottom) 0.3, 0.5 and 0.7 w/w. The temperature difference over the cell thickness is of $\Delta\mathbf{T} = +\mathbf{20}\,^\circ\mathbf{C}$ (heating from above) for the left column, and $\Delta\mathbf{T} = -\mathbf{20}\,^\circ\mathbf{C}$ (heating from below) for the right one

A first series of qualitative observations at the average temperature of 25 °C have been performed for three different concentrations by applying to the samples either a stabilizing or a destabilizing temperature gradient. A stabilizing temperature gradient generates a density gradient parallel to the gravity acceleration. It is thus obtained by heating from above $\Delta T = +20$ K and with a positive thermal expansion coefficient α. A destabilizing temperature gradient generates a density gradient anti-parallel to the gravity acceleration. It is thus obtained by heating from below $\Delta T = -20$ K.

As visible in Fig. 4, samples for $C = 0.3$, 0.5 and 0.7 w/w have been stressed by positive and negative temperature differences while shadowgraph images were recorded in order to evaluate the presence of convective patterns after reaching the steady state of the Soret separation. The patterns obtained by heating the samples for $C = 0.3$ w/w from above (thermally stable),

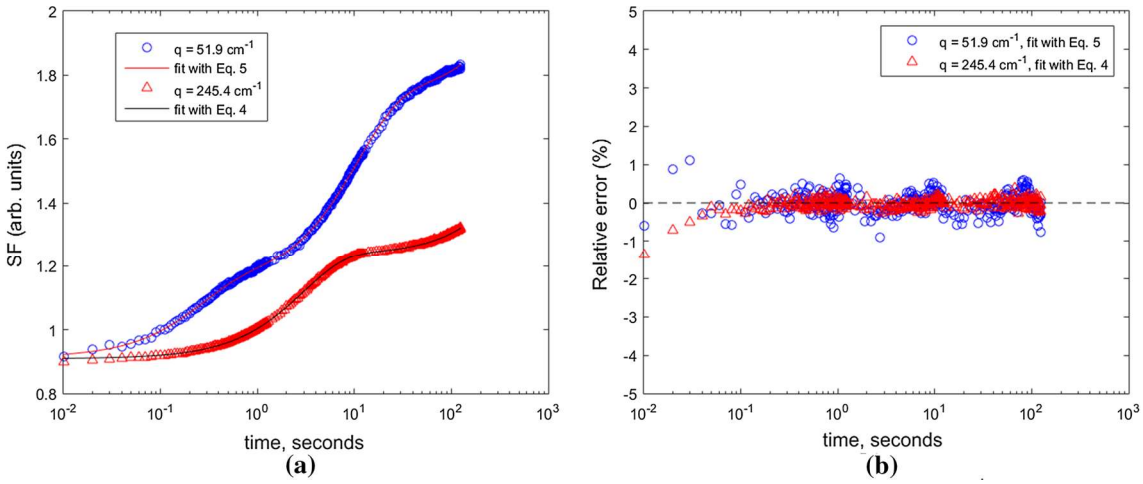

Fig. 5 **a** Concatenated structure functions for different wave numbers of the thermodiffusion experiment carried out at temperature difference of +20 °C, mean temperature of 25 °C and $C = 0.3$ w/w. **b** Corresponding relative errors between data points and the theoretical models

are featureless at the steady state, thus suggesting a stable configuration. In the patterns visible at $C = 0.5$ w/w slight features appear, thus suggesting a moderate convective instability taking place within the fluid. This means that the density gradient originated by the concentration gradient is slightly larger in modulus than the density gradient generated by the temperature gradient. Finally, strong convective patterns appear in the case for $C = 0.7$ w/w thus confirming the negative sign of the Soret coefficient for the mixture TEG/water for concentration of TEG larger than 0.5 w/w.

For the cases when a stable configuration was reached at the steady state, series of images were recorded in order to analyse the NEFs and extract the transport properties of the mixture as described above. Series of 2500 images of 2048×2048 pix^2 were recorded at 100 Hz, 10 Hz and 1 Hz at different mean temperatures of 20, 25 and 30 °C.

The SFs were calculated and concatenated according to a procedure already presented in our previous work [36,37]. The resulting SFs obtained for the concentration of 0.3 w/w of TEG and the average temperature of 25 °C is shown in Fig. 5a.

The minimum accessible wave number is given by $q_{min} = 2\pi/L$, L being the side of the image in the real space. For the acquired images, $L = 1.33$ cm, so that $q_{min} = 4.72\,\mathrm{cm}^{-1}$. The theoretical maximum frequency is $q_{max} = (N_{pix}/2) \cdot q_{min} = 4833\,\mathrm{cm}^{-1}$, N_{pix} being the number of the pixels along one side of the images.

By the analysis of the concatenated SFs, like those shown in Fig. 5a, we could determine that a double exponential decay is present for wave numbers $q < 200\,\mathrm{cm}^{-1}$, while a simple exponential decay is present for wave numbers $q > 200\,\mathrm{cm}^{-1}$. In Fig. 5b the relative errors residuals between the experimental points and the theoretical models for wave numbers $q = 51.9\,\mathrm{cm}^{-1}$ and $q = 245.4\,\mathrm{cm}^{-1}$ are reported. The values are typically smaller than 1% and random spread around zero, indicating a good match between models and experimental data. Following these observations, the SFs have been fitted by Eq. 5 for wave numbers smaller than 200 cm^{-1} and Eq. 4 for larger ones. As anticipated, the resulting values for the parameters $E(q)$ and $F(q)$ turned out to be negligible, as an indirect confirmation that the images have been acquired at the steady state of the thermodiffusion experiment. In this case, the quantity $A(q)/C(q)$ can be calculated and provides a useful indication of the signal-to-noise ratio of the measurement. In Fig. 6, the values of such ratio are reported for measurements performed at $C = 0.3$ and 0.7 w/w and for different average temperatures.

The oscillations visible in the graphs are related to the shadowgraph transfer function $T(q)$ that vanishes at specific wave number. The horizontal line visible in Fig. 6 stands for the threshold value of 0.05 above which we consider that a shadowgraph measurement cannot provide reliable results [43,44]. After such analysis, we decided to perform the fitting in the common wave number range from 30 to 450 cm^{-1} for both mixtures, thus spanning more than one decade in wave numbers.

The decay times obtained by fitting data points with the model functions described above are reported in Fig. 7. In the latter, results are shown for the two concentrations of $C = 0.3$ and 0.7 w/w at the three different temperatures.

In both cases, two time decays can be identified for most of the wave numbers. The fastest modes, corresponding to the smaller value of the time decay, are related to the decay of thermal fluctuations. Data points obtained for $C = 0.7$ w/w are more scattered than those obtained for $C = 0.3$ w/w. A possible explanation can be related to the negative Soret coefficient and the consequent coexistence of a stable density gradient stemming from concentration profile and an unstable one stemming from the temperature profile. Nevertheless, two diffusive regimes are clearly visible in both graphs, as indicated by the decay time behavior proportional to q^{-2}. On the contrary, the gravitational effect is almost not observable and no clear maximum can be detected for the thermal modes. Nevertheless,

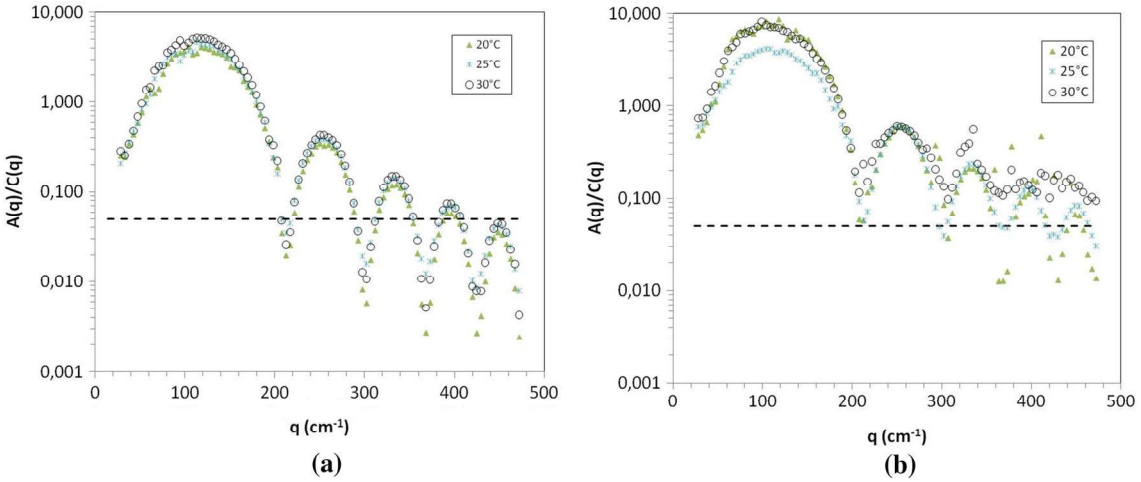

Fig. 6 Ratio between the static structure factor and the signal background as a function of the wave number and the mean temperature for the thermodiffusion experiments carried out at temperature difference of **a** +20 °C for $C = 0.3$ w/w and **b** −20 °C for $C = 0.7$ w/w

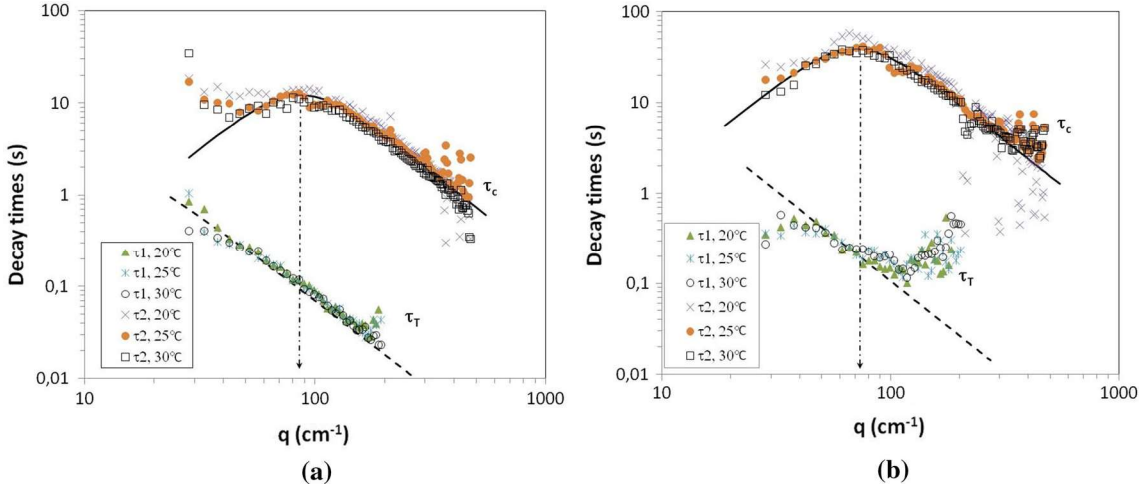

Fig. 7 Decay times of the t-NEFs (τ_T) and the c-NEFs (τ_C) as a function of the wave number and for three different values of the mean temperature for the thermodiffusion experiments carried out at temperature difference of a) +20 °C for $C = 0.3$ w/w and b) -20 °C for $C = 0.7$ w/w. The continuous lines represent the fitting of the c-NEFs at 25 °C with Eq. 6. The dashed lines represents the fitting of the t-NEFs at 25 °C with the asymptotic behavior of Eq. 9

fitting the thermal time decays with the asymptotic behaviour of Eq. 9 can provide a reliable estimation of the thermal diffusivity a_T. The slowest modes are then related to the decay of concentration fluctuations. For the two concentrations, a mass diffusive mode can be detected as well as the effect of gravity reducing the time decay of NEFs for wave numbers smaller than a characteristic value (q_c). Fitting the concentration time decays with Eq. 6, provides the mass diffusion coefficients D and the cut-off wave numbers q_c at different mean temperatures. At the smallest wavenumbers for $C = 0.3$ w/w, a deviation between the experimental points and the gravity behaviour predicted by Eq. 6 is noticeable. Such behaviour has already been observed on polymer-based systems (slowing-down of the larger fluctuations) [36,37], and can be attributed to the coupling between different modes, and can also explain why the gravitational behaviour of the thermal fluctuations is not detectable. With the values of D, q_c, β and ν the Soret diffusion coefficients S_T are calculated through Eq. 7. The resulting values of the transport coefficients obtained by thermodiffusion experiments are reported in Table 2.

Uncertainties for the mass diffusion coefficients, cut-off wave numbers and thermal diffusivities are those given by the fitting routine. Uncertainties for the Soret coefficients are calculated by error propagation. The values reported in Table 2 show that the diffusion coefficient increases with the temperature for the two TEG concentrations, which is a reasonable behaviour as fluid viscosity typically decreases with increasing temperature and the mass diffusion coefficient is inversely pro-

Journal: 10189 MS: 0171 ☐ TYPESET ☐ DISK ☐ LE ☐ CP Disp.:2022/2/24 Pages: 15 Layout: EPJE

Table 2 Diffusion coefficients D, cut-off wave number $\mathbf{q_c}$, thermal diffusivity a_T and Soret coefficient $S_T$obtained by thermodiffusion experiments of TEG/water mixtures at different mean temperatures T and TEG mass fraction concentration C

T (°C)	D ($\times 10^{-6}$ cm^2/s)	q_c (cm^{-1})	a_T ($\times 10^{-4}$ cm^2/s)	S_T ($\times 10^{-3}$ K^{-1})
$C = 0.3$ w/w				
20	4.79 ± 0.12	86.7 ± 1.1	13.1 ± 0.4	2.3 ± 0.3
25	5.46 ± 0.15	86.8 ± 1.3	13.1 ± 0.2	2.3 ± 0.3
30	6.4 ± 0.3	84 ± 2	13.29 ± 0.13	2.0 ± 0.4
$C = 0.7$ w/w				
20	2.02 ± 0.08	70.7 ± 1.5	9.4 ± 0.2	- 3.8 ± 0.6
25	2.6 ± 0.1	70.3 ± 1.4	9.4 ± 0.4	- 3.9 ± 0.6
30	2.73 ± 0.06	70.5 ± 0.8	9.4 ± 0.4	- 3.4 ± 0.3

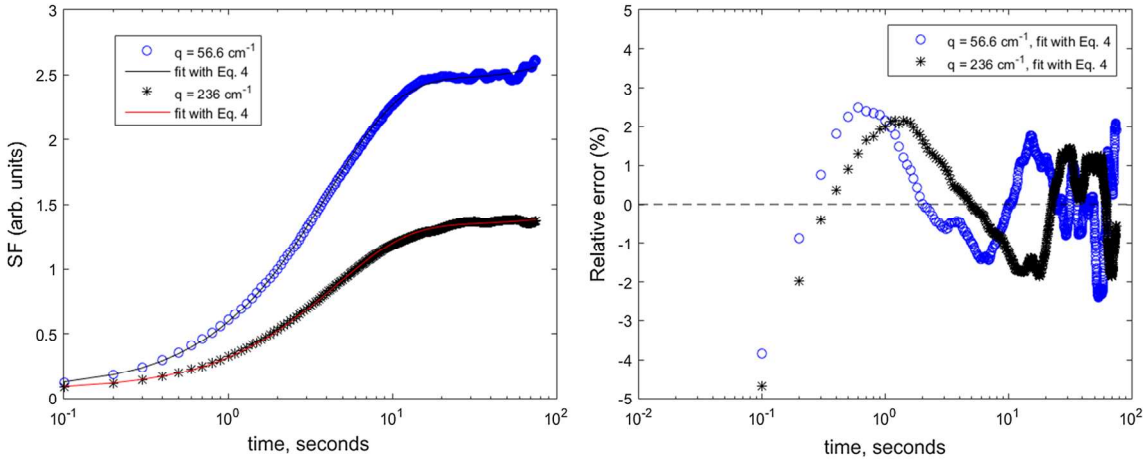

Fig. 8 **a** Structure function for different wave numbers of the free-diffusion experiment carried out at the mean concentration of $C = 0.5$ w/w, difference of concentration $\Delta\mathbf{C} = \mathbf{02}$ w/w between the bottom and top layer solutions, mean temperature of 25 °C and 80 minutes after closing the valves. **b** Corresponding relative errors between data points and the theoretical models

portional to the fluid viscosity, following the Stokes-Einstein relation. Taking into account the uncertainties, the values of the Soret coefficient do not change over the investigated temperature range for C =0.3 w/w, and a clear trend is not observed for $C = 0.7$ w/w.

4.2 Free-diffusion experiments

For the concentration $C = 0.5$ w/w it was not possible to obtain a reliable measurement of the mass diffusion coefficient from the thermodiffusion experiments, due to the negative value of the Soret coefficient, close to zero [18]. Therefore, free-diffusion experiments were performed at the average temperatures of 20, 25 and 30 °C. Further experiments were performed in free-diffusion for the concentration $C = 0.7$ w/w in order to confirm the results obtained by thermodiffusion, given the fact that this is the first time that a shadowgraph investigation of NEFs is performed on a sample with negative Soret coefficients to extract its transport coefficients. In the case of a free-diffusion experiment, the diffusion cell is filled as described in Sect. 2.2. Briefly, the diffusion cell is first filled with the less dense solution and subsequently, the less dense and the denser solution fills about half of the cell, the valves are closed and the free-diffusion process starts. In the case of the isothermal diffusion experiment, only one mode is expected to be measured corresponding to the relaxation of c-NEFs in the fluid mixture. The time decays are therefore expected to span a narrower range of time, so that only one series of images of 1024×1024 pix^2 is acquired at a frequency of 10 Hz. In this simpler case, the SFs are directly calculated by the DDA algorithm without further processing, as shown in Fig. 8a for the average concentration of $C = 0.5$ w/w, a difference of concentration of $\Delta C = C_1 - C_2 = 0.2$ w/w between the two superposed fluid layers, a homogeneous temperature of 25 °C, and 80 minutes after closing the valves.

In Figure 8b we report the relative errors between the calculated SF and the fitting by a mono-exponential model of the *ISF* (Eq. 4). At long correlation times the residuals are slightly larger, but every time smaller than 3%, so that data points can be fitted through Eq. 4 for the entire range of wave numbers. In Fig. 9 the signal-

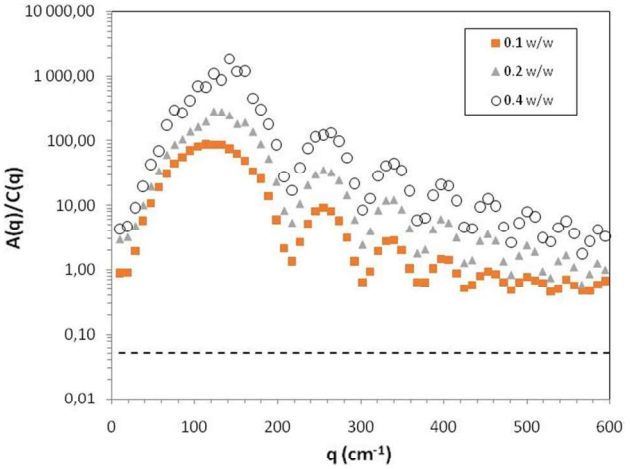

Fig. 9 Ratio between the static structure factor and the signal background as a function of the wave number for the free-diffusion experiments carried out at mean concentration of $C = 0.5$ w/w, and for different concentration differences between the bottom and the top layers, at 25 °C and 80 minutes after closing the valves

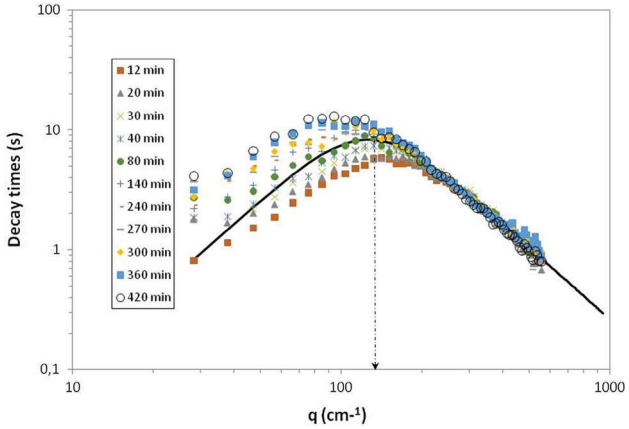

Fig. 10 Decay times of the c-NEFs as a function of the wave numbers for different times after closing the inlet/outlet valves for the free-diffusion experiment carried out at $C = 0.5$ w/w, difference of concentration $\Delta C = 0.2$ w/w and $T = 25$ °C. The continuous black line corresponds to the curve got by fitting Eq. 6 to data points obtained 80 minutes after starting the free-diffusion experiment

to-noise ratio is shown for the sample with $C = 0.5$ w/w and the homogeneous temperature $T = 25$ °C for images taken 80 minutes after closing the inlet/outlet valves. The values are reported for three different values of the concentration difference ΔC =0.1, 0.2 and 0.4 w/w. By comparing Figs. 6 and 9, it is evident that the signal obtained in the case of free-diffusion experiments is much larger than the one obtained in the thermodiffusion experiments. That is due to the fact that the overall signal intensity is proportional to the square of the density gradient, that is much larger in the free-diffusion case due to the different shape of the concentration profile. The optical signal, however, is integrated over the entire fluid vertical thickness, which reduces the overall difference in signal intensity. As visible from Fig. 9, the signal also increases with increasing concentration difference and distance for ΔCbetween 0.1 and 0.2 w/w. However, it is approximatively the same in a log-log graph whatever the distance for ΔC between 0.2 and 0.4 w/w, which is coherent with a quadratic dependence of the signal to the concentration difference.

In the case of free-diffusion experiments, we decided to further analyse data points in the wave number range from 30 to 600 cm^{-1}, within which the signal-to-noise ratio indicator keeps above the threshold. In Fig. 10 we report the decay times obtained from fitting the SFs as a function of the wave number q and for different times after closing the inlet/outlet valves. The graph corresponds to a sample with $C = 0.5$ w/w, $\Delta C = 0.2$ w/w and $T = 25$ °C. As stated before, only one mode can be detected corresponding to the decay of c-NEFs. By fitting the decay times through Eq. 6 we can obtain a measurement of the roll off wave number q_c and the mass diffusion coefficient D.

For all the times, the relaxation time curve has a bell-shape in the log-log plot of τ vs. q. As already reported in a number of publications, the right part of such curves for large wave numbers corresponds to the diffusive regime of c-NEFs. All curves collapse onto a single one for large wave numbers, because the mass diffusion coefficient remains constant during the free-diffusion process. This can be clearly observed also in Fig. 11-a, where the mass diffusion coefficients obtained after fitting time decays through Eq. 6 are shown as a function of the normalised time (i.e. t/τ_d, τ_d calculated using reference values of D). Moreover, the diffusion coefficient does not change with respect to the applied concentration difference ΔC. All data shown in Fig. 11 are relative to the average concentration $C = 0.5$ w/w at $T = 25$ °C. On the contrary, the position of the maximum of the decay time bell-shape, q_c, decreases with time, as shown Fig. 11-b.

The values obtained for the mass diffusion coefficient D are nicely centred around the literature value obtained by Optical Beam Deflection (OBD) [18], that is represented by a horizontal dashed line in Fig. 11a. The values obtained for $\Delta C = 0.1$ w/w are somewhat more scattered, which mirrors the smaller signal-to-noise ratio, also visible in Fig. 9. Moreover, the measurement error is increased for times close to the diffusive time of the cell, because, again, the signal-to-noise ratio decreases due to the decrease of the concentration gradient. The values obtained for the mass diffusion coefficient remain almost constant as a function of time and do not depend on the concentration difference imposed at the beginning of the experiment. Conversely, the cut-off wave number decreases with time and with the concentration difference according to Eq. 8. Fitting data point with a power law and free exponent provides a value of −0.11, rather close to the theoretical value of -0.125.

The experiments reported in Fig. 12 have been performed with average concentration $C = 0.5$ w/w and

Journal: 10189 MS: 0171 ☐ TYPESET ☐ DISK ☐ LE ☐ CP Disp.:2022/2/24 Pages: 15 Layout: EPJE

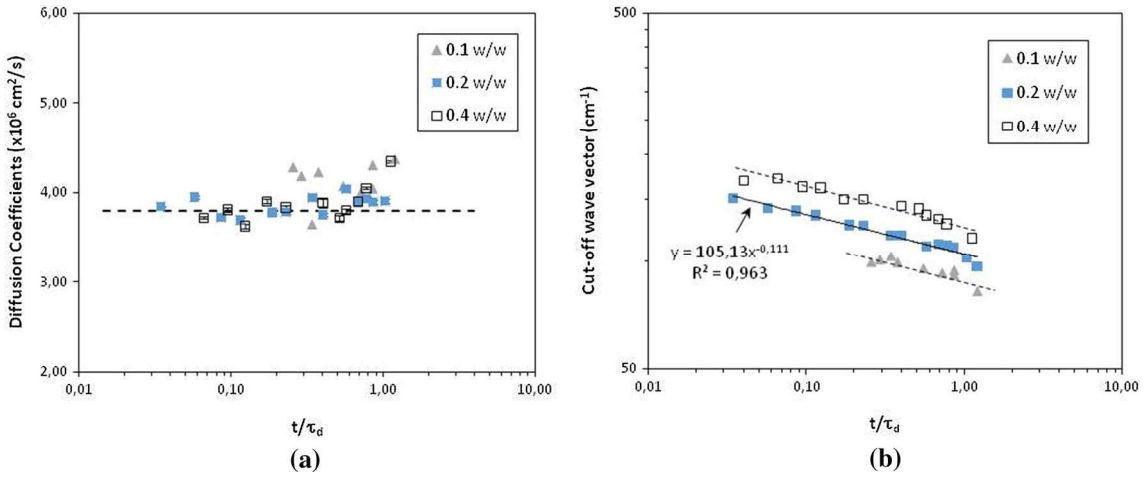

Fig. 11 **a** Mass diffusion coefficient D and **b** cut-off wave number q_c as a function of the normalized time for different concentration differences for the free-diffusion experiments carried out at $C = 0.5$ w/w and $T = 25$ °C

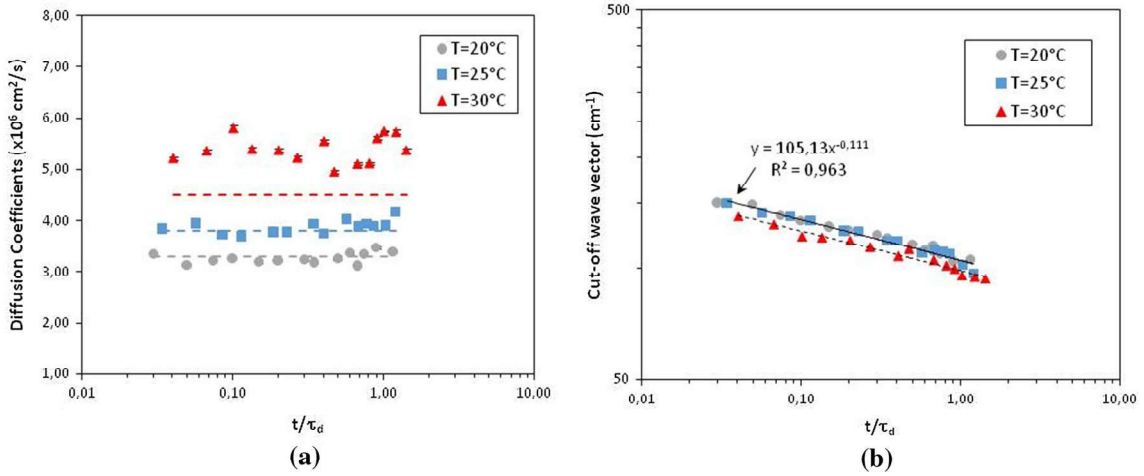

Fig. 12 **a** Mass diffusion coefficient and **b** cut-off wave number as a function of the normalized time for different temperatures for the free-diffusion experiments with $C = 0.5$ w/w and $\Delta C = 0.2$ w/w

concentration difference $\Delta C = 0.2$ w/w. In Fig. 12a we report the values of the mass diffusion coefficient and the cut-off wave number as a function of the normalised time and for different values of the homogeneous temperature. In Fig. 12b we report the values of the cut-off wave number as a function of the normalized time in the same conditions.

In Figure 12a, the horizontal dashed lines provide a visual reference of the values of the mass diffusion coefficient obtained by OBD and reported in the literature [18]. The data points for $T = 20$ and 25 °C are in very good agreement with the literature values, however those obtained at 30 °C show a 10% difference with respect to the literature one. In Fig. 12b we can see that the wave numbers follow a power law dependence upon reduced time with an exponent close to the theoretical value of -0.125 for all the three investigated temperatures.

In Table 3 we provide the obtained values of the mass diffusion coefficients as obtained by the free-diffusion experiments performed at the two average concentrations of $C = 0.5$ and 0.7 w/w, at the three different homogeneous temperatures of $T = 20$, 25 and 30 °C. For the average concentration of $C = 0.7$ w/w, the studied concentration difference between bottom and top solutions was $\Delta C = 0.2$ w/w. The corresponding mass diffusion coefficients obtained at different temperatures are consistent or even compatible to those summarized in Table 2 for the same TEG concentration of 0.7 w/w.

The uncertainties reported in Table 3 correspond to the standard deviation with respect to the average value including the measurements obtained at different normalised times. In the case of the measurements performed at $C = 0.5$ w/w, we averaged data obtained for $\Delta C = 0.2$ and 0.4 w/w.

Journal: 10189 MS: 0171 ☐ TYPESET ☐ DISK ☐ LE ☐ CP Disp.:2022/2/24 Pages: 15 Layout: EPJE

Table 3 Mass diffusion coefficients D obtained by free-diffusion experiments at mean concentration C in mass fraction of TEG and homogeneous temperature T

D ($\times 10^{-6}$ cm^2/s)		
T (°C)	$C = 0.5$ w/w	$C = 0.7$ w/w
20	3.27 ± 0.10	2.15 ± 0.16
25	3.86 ± 0.14	2.32 ± 0.06
30	5.4 ± 0.3	3.00 ± 0.13

5 Conclusion

In this paper, we have measured the mass diffusion and the thermodiffusion coefficients of triethylene glycol and water binary mixtures at different concentrations and average temperatures. Up to our best knowledge, this is the first time that the method combining dynamic shadowgraphy and the analysis of non-equilibrium fluctuations is used to measure the transport properties of a fluid mixture in a free-diffusion experiment. It is also the first time that the method is applied to measure the mass diffusion and the Soret coefficients in a thermodiffusion experiment for a sample of negative Soret coefficient as it is the case for the triethylene glycol/water mixture at $C = 0.7$ w/w.

The obtained values of mass diffusion coefficient are consistent with data available in the literature for the range of temperature investigated in this study from 20 to 30 °C. The mass diffusion coefficients of 0.7 w/w triethylene glycol/water mixture measured at different temperatures through free-diffusion experiments are consistent with those determined by thermodiffusion experiments. An increase of the mass diffusion coefficient as a function of the average temperature is detected. On the other hand, the thermodiffusion coefficient appears to be independent of the average temperature of the sample at 0.3 w/w triethylene glycol concentration. Soret coefficients have been determined with a relative uncertainty of 10% without prior knowledge of optical contrast factors.

Acknowledgements This work was developed in the framework of the cooperative project DCMIX (AO-2009-0858/1056) of the European Space Agency (ESA) and the Russian Space Agency (Roscosmos). The shadowgraphy measurements are supported by the ESA project GIANT FLUCTUATIONS and the ESA-MAP project TechNES (Grant 4000128933/19/NL/PG). We acknowledge financial support from the CNES and from the E2S UPPA Hub Newpores and the Industrial Chair CO2ES supported by the Investissements d'Avenir French programme managed by ANR (ANR-16-IDEX-0002), and BRGM and TotalEnergies. L. García-Fernández is thankful to Comunidad de Madrid for the financial support of the postdoctoral researcher contract "Atracción de Talento Investigador (2019-T2/AMB-15912)".

Author contribution statement

H.B., M.A., A.L. and F.C. conceived the project and the experiments. A.T.N. conducted the experiments. H.B., A.T.N., L.G.F. and F.C. wrote the manuscript. All the authors analyzed and discussed the content of the paper.

References

1. F. Montel, J. Bickert, A. Lagisquet, G. Galliero, Initial state of petroleum reservoirs: a comprehensive approach. J. Petrol. Sci. Eng. **58**(3), 391–402 (2007). https://doi.org/10.1016/j.petrol.2006.03.032
2. H. Guo, Q. Zhou, Z. Wang, Y. Huang, Soret effect on the diffusion of CO2 in aqueous solution under high-pressure. Int. J. Heat Mass Trans. **117**, 966–971 (2018). https://doi.org/10.1016/j.ijheatmasstransfer.2017.10.058
3. W. Köhler, K.I. Morozov, The soret effect in liquid mixtures - a review. J. Non-Equilibrium Thermodynam. **41**(3), 151–197 (2016). https://doi.org/10.1515/jnet-2016-0024
4. J.K. Platten et al., Benchmark values for the Soret, thermal diffusion and diffusion coefficients of three binary organic liquid mixtures. Philosophical Magazine **83**(17–18), 1965–1971 (2003). https://doi.org/10.1080/0141861031000108204
5. H. Bataller, T. Triller, B. Pur, W. Köhler, J.M. Ortiz de Zárate, F. Croccolo, Dynamic analysis of the light scattered by the non-equilibrium fluctuations of a ternary mixture of polystyrene-toluene-n-hexane. Eur. Phys. J. E **40**(3), 35 (2017). https://doi.org/10.1140/epje/i2017-11522-8
6. H. Bataller, C. Giraudet, F. Croccolo, J.M. Ortiz de Zárate, Analysis of non-equilibrium fluctuations in a ternary liquid mixture. Microgravity Sci. Technol. **28**(6), 611–619 (2016). https://doi.org/10.1007/s12217-016-9517-6
7. M.M. Bou-Ali et al., Benchmark values for the Soret, thermodiffusion and molecular diffusion coefficients of the ternary mixture tetralin+isobutylbenzene+n-dodecane with 0.8–0.1-0.1 mass fraction. Eur. Phys. J. E (2015). https://doi.org/10.1140/epje/i2015-15030-7
8. A. Ahadi, S.V. Varenbergh, M.Z. Saghir, Measurement of the Soret coefficients for a ternary hydrocarbon mixture in low gravity environment. J. Chem. Phys. **138**(20), 204201 (2013). https://doi.org/10.1063/1.4802984
9. A. Mialdun, I. Ryzhkov, O. Khlybov, T. Lyubimova, V. Shevtsova, Measurement of Soret coefficients in a ternary mixture of toluene-methanol-cyclohexane in convection-free environment. J. Chem. Phys. **148**(4), 044506 (2018). https://doi.org/10.1063/1.5017716
10. A. Mialdun, V. Shevtsova, Temperature dependence of Soret and diffusion coefficients for toluene-cyclohexane mixture measured in convection-free environment. J. Chem. Phys. **143**(22), 224902 (2015). https://doi.org/10.1063/1.4936778
11. T. Triller et al., Thermodiffusion in Ternary Mixtures of Water/Ethanol/Triethylene Glycol: First Report on the

DCMIX3-Experiments Performed on the International Space Station. Microgravity Sci. Technol. **30**(3), 295–308 (2018). https://doi.org/10.1007/s12217-018-9598-5
12. M. Touzet, G. Galliero, V. Lazzeri, M.Z. Saghir, F. Montel, J.-C. Legros, Thermodiffusion: from microgravity experiments to the initial state of petroleum reservoirs. Comptes Rendus Mécanique **339**(5), 318–323 (2011). https://doi.org/10.1016/j.crme.2011.03.008
13. G. Galliero et al., Thermodiffusion in multicomponent n-alkane mixtures. npj Micrograv. **3**(1), 1–7 (2017). https://doi.org/10.1038/s41526-017-0026-8
14. S. VanVaerenbergh, S. Srinivasan, M.Z. Saghir, Thermodiffusion in multicomponent hydrocarbon mixtures: experimental investigations and computational analysis. J. Chem. Phys. **131**(11), 114505 (2009). https://doi.org/10.1063/1.3211303
15. G. Galliero et al., Impact of thermodiffusion on the initial vertical distribution of species in hydrocarbon reservoirs. Micrograv. Sci. Technol. **28**(2), 79–86 (2016). https://doi.org/10.1007/s12217-015-9465-6
16. P. Baaske et al., The NEUF-DIX space project - Non-EquilibriUm Fluctuations during DIffusion in compleX liquids'. Eur. Phys. J. E (2016). https://doi.org/10.1140/epje/i2016-16119-1
17. M. Braibanti et al., European space agency experiments on thermodiffusion of fluid mixtures in space. Eur. Phys. J. E **42**(7), 86 (2019). https://doi.org/10.1140/epje/i2019-11849-0
18. M. Schraml et al., The Soret coefficients of the ternary system water/ethanol/triethylene glycol and its corresponding binary mixtures. Eur. Phys. J. E **44**(10), 128 (2021). https://doi.org/10.1140/epje/s10189-021-00134-6
19. J. M. Ortiz de Zárate and J. V. Sengers, Hydrodynamic Fluctuations in Fluids and Fluid Mixtures - 1st Edition'. https://www.elsevier.com/books/hydrodynamic-fluctuations-in-fluids-and-fluid-mixtures/ortiz-de-zarate/978-0-444-51515-5 (accessed Sep. 30, 2021)
20. F. Croccolo, J.M. Ortiz de Zárate, J.V. Sengers, Non-local fluctuation phenomena in liquids. Eur. Phys. J. E **39**(12), 125 (2016). https://doi.org/10.1140/epje/i2016-16125-3
21. A. Vailati, M. Giglio, Giant fluctuations in a free diffusion process. Nature **390**(6657), 262–265 (1997). https://doi.org/10.1038/36803
22. P.N. Segrè, R. Schmitz, J.V. Sengers, Fluctuations in inhomogeneous and nonequilibrium fluids under the influence of gravity. Physica A: Statistical Mech. Appl. **195**(1), 31–52 (1993). https://doi.org/10.1016/0378-4371(93)90252-Y
23. P.N. Segrè, J.V. Sengers, Nonequilibrium fluctuations in liquid mixtures under the influence of gravity. Physica A: Statistical Mech. Appl. **198**(1), 46–77 (1993). https://doi.org/10.1016/0378-4371(93)90183-5
24. E. Bouty, CH. SORET. – Sur l'état d'équilibre que prend, au point de vue de sa concentration, une dissolution saline primitivement homogène, dont deux parties sont portées à des températures différentes; Archives de Genève, 3e periode, t. II, p. 48; 1879. J. Phys. Theor. Appl. **9**(1), 331–332 (1880). https://doi.org/10.1051/jphystap:018800090033101
25. F. Croccolo, D. Brogioli, A. Vailati, M. Giglio, D.S. Cannell, Nondiffusive decay of gradient-driven fluctuations in a free-diffusion process. Phys. Rev. E **76**(4), 041112 (2007). https://doi.org/10.1103/PhysRevE.76.041112
26. F. Croccolo, H. Bataller, F. Scheffold, A light scattering study of non equilibrium fluctuations in liquid mixtures to measure the Soret and mass diffusion coefficient. J. Chem. Phys. **137**(23), 234202 (2012). https://doi.org/10.1063/1.4771872
27. W. Wu, J.H. Jander, M.H. Rausch, A.P. Fröba, C. Giraudet, Simultaneous determination of multiple transport properties over a wide range of temperatures and pressures from the analysis of non-equilibrium fluctuations by the shadowgraph method. J. Chem. Phys. **153**(14), 144201 (2020). https://doi.org/10.1063/5.0024503
28. C. Giraudet, H. Bataller, F. Croccolo, High-pressure mass transport properties measured by dynamic near-field scattering of non-equilibrium fluctuations. Eur. Phys. J. E **37**(11), 107 (2014). https://doi.org/10.1140/epje/i2014-14107-1
29. F. Croccolo, D. Brogioli, Quantitative Fourier analysis of schlieren masks: the transition from shadowgraph to schlieren. Appl. Opt. AO **50**(20), 3419–3427 (2011). https://doi.org/10.1364/AO.50.003419
30. S.P. Trainoff, D.S. Cannell, Physical optics treatment of the shadowgraph. Phys. Fluids **14**(4), 1340–1363 (2002). https://doi.org/10.1063/1.1449892
31. I. Lizarraga, C. Giraudet, F. Croccolo, M.M. Bou-Ali, H. Bataller, Mass diffusion and thermal diffusivity of the Decane-pentane mixture under high pressure as a ground-based study for SCCO project. Micrograv. Sci. Technol. **28**(5), 545–552 (2016). https://doi.org/10.1007/s12217-016-9506-9
32. F. Croccolo, D. Brogioli, A. Vailati, Cylindrical flowing-junction cell for the investigation of fluctuations and pattern-formation in miscible fluids. Rev. Sci. Instruments **90**(8), 085109 (2019). https://doi.org/10.1063/1.5112778
33. G. Cerchiari, F. Croccolo, F. Cardinaux, F. Scheffold, Note: Quasi-real-time analysis of dynamic near field scattering data using a graphics processing unit. Rev. Sci. Instruments **83**(10), 106101 (2012). https://doi.org/10.1063/1.4755747
34. M. Norouzisadeh, M. Chraga, G. Cerchiari, F. Croccolo, 'The modern structurator: Increased performance for calculating the structure function.', *submitted*
35. J.M. Ortiz de Zárate, C. Giraudet, H. Bataller, F. Croccolo, Non-equilibrium fluctuations induced by the Soret effect in a ternary mixture'. Eur. Phys. J. E (2014). https://doi.org/10.1140/epje/i2014-14077-2
36. F. Croccolo, L. García-Fernández, H. Bataller, A. Vailati, J.M. Ortiz de Zárate, Propagating modes in a binary liquid mixture under thermal stress. Phys. Rev. E **99**(1), 012602 (2019). https://doi.org/10.1103/PhysRevE.99.012602
37. L. García-Fernández, P. Fruton, H. Bataller, J.M. Ortiz de Zárate, F. Croccolo, Coupled non-equilibrium fluctuations in a polymeric ternary mixture'. Eur. Phys. J. E (2019). https://doi.org/10.1140/epje/i2019-11889-4
38. D. J. Higham, N. J. Higham, *MATLAB Guide, Third Edition*. SIAM, UK (2016)

39. F. Croccolo, D. Brogioli, A. Vailati, M. Giglio, D.S. Cannell, Use of dynamic schlieren interferometry to study fluctuations during free diffusion. Appl. Opt., AO **45**(10), 2166–2173 (2006). https://doi.org/10.1364/AO.45.002166
40. I. Lizarraga, F. Croccolo, H. Bataller, M.M. Bou-Ali, Soret coefficient of the n-dodecane-n-hexane binary mixture under high pressure'. Eur. Phys. J. E (2017). https://doi.org/10.1140/epje/i2017-11520-x
41. F. Croccolo, D. Brogioli, A. Vailati, M. Giglio, D.S. Cannell, Effect of gravity on the dynamics of nonequilibrium fluctuations in a free-diffusion experiment. Ann New York Acad Sci **1077**(1), 365–379 (2006). https://doi.org/10.1196/annals.1362.030
42. J.C. Legros et al., Investigation of Fickian diffusion in the ternary mixtures of water-ethanol-triethylene glycol and its binary pairs. Phys. Chem. Chem. Phys. **17**(41), 27713–27725 (2015). https://doi.org/10.1039/C5CP04745E
43. K. He, M. Spannuth, J.C. Conrad, R. Krishnamoorti, Diffusive dynamics of nanoparticles in aqueous dispersions. Soft Matter **8**(47), 11933–11938 (2012). https://doi.org/10.1039/C2SM26392K
44. M.S. Safari, M.A. Vorontsova, R. Poling-Skutvik, P.G. Vekilov, J.C. Conrad, Differential dynamic microscopy of weakly scattering and polydisperse protein-rich clusters. Phys. Rev. E **92**(4), 042712 (2015). https://doi.org/10.1103/PhysRevE.92.042712